COMMUNICATION

Check for updates

Tailoring the multistability of origami-inspired, buckled magnetic structures *via* compression and creasing†

Yi Li,‡[a] Samuel J. Avis, ‡[b] Teng Zhang, *[c] Halim Kusumaatmaja *[b] and Xueju Wang *[ad]

Origami-inspired multistable structures are gaining increasing interest because of their potential applications in fields ranging from deployable structures to reconfigurable microelectronics. The multistability of such structures is critical for their applications but is challenging to manipulate due to the highly nonlinear deformations and complex configurations of the structures. Here, a comprehensive experimental and computational study is reported to tailor the multistable states of origami-inspired, buckled ferromagnetic structures and their reconfiguration paths. Using ribbon structures as an example, a design phase diagram is constructed as a function of the crease number and compressive strain. As the crease number increases from 0 to 7, the number of distinct stable states first increases and then decreases. The multistability is also shown to be actively tuned by varying the strain from 0% to 40%. Furthermore, analyzing energy barriers for reconfiguration among the stable states reveals dynamic changes in reconfiguration paths with increasing strains. Guided by studies above, diverse examples are designed and demonstrated, from programmable structure arrays to a soft robot. These studies lay out the foundation for the rational design of functional, multistable structures.

New concepts

An outstanding challenge in the field of origami-inspired multistable structures is to actively control the number of possible stable states and their reconfiguration paths. In this work, we present an integrated experimental and computational study on how they can be systematically tailored and controlled *via* two effective and easy-to-control parameters, creasing and compressive strains. Computationally, we construct a detailed design phase diagram for a representative ribbon structure showing how the number of stable states can be varied. Furthermore, we predict the reconfiguration paths and their corresponding energy barriers to transition between stable states. Experimentally, we realize origami-inspired structures composed of ferromagnetic composite thin films under various creasing and compressive strain conditions, where fast, remote reconfigurations are achieved using a portable magnet. The computational and experimental results are in excellent agreement. We believe the new insights generated from our work are valuable for diverse applications exploiting origami-inspired structures. For instance, here we design and demonstrate programmable structure arrays, a biomimetic insect, and an origami robot that can be actuated by remote magnetic forces.

1. Introduction

Origami, the ancient art of folding two-dimensional (2D) thin sheets along predefined creases to create three-dimensional (3D) objects,[1–3] has inspired the design of many engineering structures for a wide range of applications, including

a Department of Materials Science and Engineering, University of Connecticut, Storrs, CT, 06269, USA. E-mail: xueju.wang@uconn.edu

b Department of Physics, Durham University, Durham, DH1 3LE, UK. E-mail: halim.kusumaatmaja@durham.ac.uk

c Department of Mechanical and Aerospace Engineering, BioInspired Syracuse, Syracuse University, Syracuse, NY, 13244, USA. E-mail: tzhang48@syr.edu

d Polymer program, Institute of Materials Science, University of Connecticut, Storrs, CT 06269, USA

† Electronic supplementary information (ESI) available. See DOI: 10.1039/d1mh01152a

‡ These authors contributed equally to this work.

deployable systems,[4–6] self-folding machines,[7] reconfigurable metamaterials,[8–10] and DNA origami.[11] For those applications, a key design feature of the structures is their ability to have multiple stable states as well as the tailoring of those states for tunability and adaptability. Existing works so far have primarily focused on bistable systems for rigid origami patterns (like the Miura folding[12] and its derivates[13]) and deformable origami (like the twisted square pattern[14]). For example, Sadeghi and Li realized rapid and reversible folding by harnessing the asymmetric bistability of designed origami structures.[15] Liu *et al.* demonstrated that a folded hyper origami, obtained by folding a piece of paper along concentric squares and their diagonals to arrive at a seemingly smooth saddle shape, exhibits bistability between two symmetric configurations.[16] More recently, Melancon *et al.* realized pressure-deployable origami structures characterized by two stable configurations – one compact and one expanded – at the meter scale.[5] Furthermore, Fang *et al.* showed that the potential energy landscapes of stacked

Miura-ori and Kresling-ori structures, and therefore their stability profiles and constitutive force–displacement relations, can be effectively tuned by embedded magnets.[17]

In addition to multistability, reconfiguration among the different stable states of origami-inspired structures in a well-controlled manner is demanded in many engineering devices and structures. Theoretical and experimental studies have been performed on reconfiguration paths in origami-inspired structures. For example, Zhai *et al.* created an origami-inspired mechanical metamaterial that can be deployed and collapsed along different configuration paths.[18] Silverberg *et al.* showed that hidden degrees of freedom in square twist origami structures give rise to a critical transition from mono- to bi-stability.[14] Moreover, significant advances have been made to improve the tunability and adaptability of origami-inspired structures by incorporating stimuli-responsive materials, such as shape memory polymers,[19–22] hydrogels,[23,24] liquid crystal elastomers,[25,26] and magnetic composites,[27] into origami-inspired structures to achieve self-folding and on-demand shape morphing under external actuations (*i.e.*, variations in temperature, light, pH, and magnetic fields). Such self-actuating materials have also enabled the assembly of origami structures at the microscale to provide opportunities for micro robotics, biomedical devices, and many others.[28–32]

Previous studies have laid solid foundations for the design and development of origami-inspired structures with bistability and tunability. One of the remaining challenges in the field of origami-inspired multistable structures is to actively control the number of possible stable states and their reconfiguration paths. Here, we demonstrate how the multistability of origami-inspired structures that are buckled from ferromagnetic composite thin films[19,33] can be tailored *via* creasing and compressive strains. Ribbon structures are chosen as an example for the study because of their very rich nonlinear buckling behavior while having a simple geometry and their potential as basic building blocks for more complicated structures, thereby providing an ideal platform to explore our design strategy. The two key control parameters, compression strains and creasing in the ribbon, are selected because they are easy to tune and

very effective in altering the multistable behaviors of the structure for real applications. In this work, the experiments are thoroughly complemented with systematic simulations. A computationally efficient discrete shell model,[34,35] which is used to simulate nonlinear deformations in thin films, is combined with a random search algorithm for energy minimization[36–38] to construct phase diagrams showing how the available stable states sensitively depend on the compressive assembly strain and the creases of structures. The predictions from the phase diagram are experimentally verified for cases at a representative constant strain (15%) and varying crease numbers, as well as those at a given crease number (3 creases) and varying strains. In addition, reconfiguration paths between the stable states are identified using energy landscape exploration algorithms,[39,40] where the transition states connecting the minima are first located with a double-ended search method, then the full pathways are computed using the downhill routes to each stable state. Our approach allows the computation of reconfiguration paths with the lowest energy barriers systematically without the need to assume a predefined path for structure morphing.[41] Fast, remote reconfigurations among the multistable states of the ferromagnetic structures are performed experimentally with a portable magnet, the pathways of which are shown to be consistent with those from computational predictions. Finally, guided by tightly integrated numerical and experimental analysis, we demonstrate diverse complex origami-inspired structures, including structure arrays that can display various patterns based on the multistability of the structural unit, a biomimetic insect, and a soft robot.

2. Results and discussions

2.1 Concept of origami-inspired, multistable 3D ferromagnetic structures

Fig. 1 schematically illustrates the assembly process and reconfiguration of origami-inspired structures compressively buckled from ferromagnetic composites.[19,42,43] Ferromagnetic
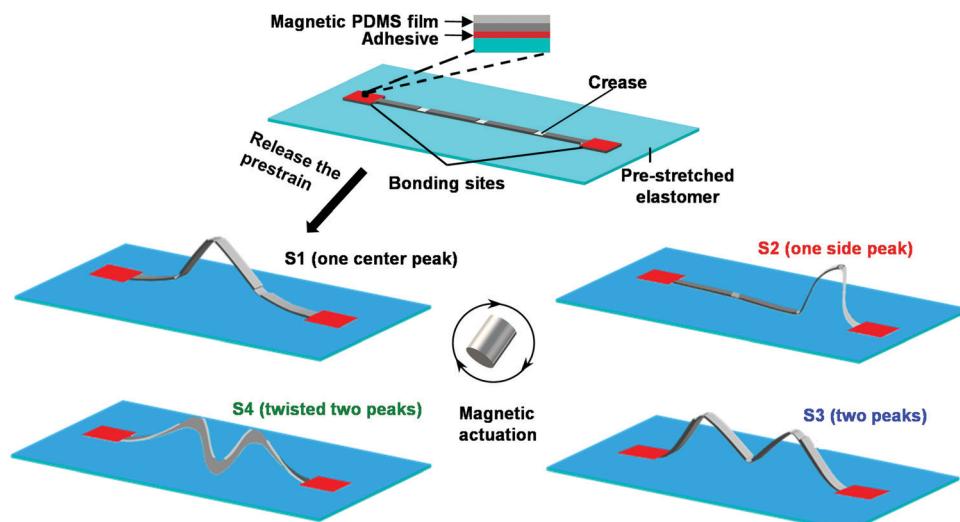
Fig. 1 Schematic illustration of the assembly and magnetic reconfiguration schemes of origami-inspired multistable ribbon structures.

composites are used as the constitutional material for the origami-inspired structures in this study to enable fast, remote reconfiguration among their mutistable states.[44–46] The scheme begins with the fabrication of soft ferromagnetic composite films (130 μm thick) made from polydimethylsiloxane (PDMS) embedded with magnetic NdFeB (neodymium–iron–boron) microparticles (∼5 μm in diameter). Laser patterning (VLS 2.30, Universal Laser System, Ansonia, CT) of the film defines the geometry and the crease of the 2D precursor with a thickness ratio of 46.15% between the crease- and non-crease regions. The location of the crease region and the reduced thickness of the corresponding segments (2.5 mm of unit length) determine the location of hinges that affect potential multistable reconfigurations.[47] To assemble origami-inspired structures, the 2D precursor is laminated onto a pre-stretched silicone elastomer substrate (Dragon skin; Smooth-on, Easton, PA), followed by the release of the pre-strain to geometrically transform the 2D precursor into the corresponding 3D structure. Under an external magnetic field generated by a manually manipulated magnet, the assembled origami-inspired structure can be reconfigured into up to four distinct stable states: state 1 (S1, one center peak), state 2 (S2, one side peak), state 3 (S3, two peaks), and state 4 (S4, twisted two peaks). Remarkably, due to their mechanical stability, the reconfigured states remain stable after the removal of the applied magnetic field.

2.2 Design phase diagram of multistable states of magnetically reconfigurable, origami-inspired structures

We first study the effect of two essential parameters, the number of creases and compressive strains, on the number and configurations of stable states by using a ribbon structure as an example. A design phase diagram, indicating the stable states of the structure with up to seven creases and at strain levels of 0–40%, is shown in Fig. 2A and serves as a theoretical foundation for the multistability design. The design phase diagram is constructed computationally by identifying the local minima in the energy landscape of the structure under various conditions of strain levels and crease numbers. To obtain these minima, we use a discrete model combined with a random search algorithm for energy minimization (see the Experimental section for full details). The discrete model has been widely used to simulate nonlinear deformation in thin films and shells, and it has been shown to be in good agreement with the more accurate but computationally more expensive finite element method.[39,48] In our computational strategy, at selected points (typically 5 different strain levels for each crease number) across the design phase diagram, the structure is randomly initialized several hundreds of times, after which it is relaxed to the minima. Once the qualitatively distinct configurations are identified, we systematically vary the compressive strain to observe the full range over which each state is stable. It is worth noting that while it is difficult to guarantee that all possible stable states are obtained, we do not find additional states when more points in the design phase diagram are sampled. Hence, we consider the identified stable states to be representative in this study.

As shown in Fig. 2A, the number of creases (n_{crease}) has notable effects on the number and configurations of stable states. To better illustrate this point, we demonstrate the available states of the structures as n_{crease} is increased from 0 to 7 under a constant compressive strain of 15% in Fig. 2B, with the computational and experimental results shown side by side. When n_{crease} is zero, i.e., a continuous ribbon structure, only S1 (one center peak) exists at all strain levels (e.g., point i). An additional asymmetric state S2 becomes available when n_{crease} rises to two at a compressive strain of 15% (point ii). A further increase to three creases causes the structure to admit state S3 (two peaks) at a strain of 15% (point iii) and S4 (twisted two peaks) at a higher strain level. As n_{crease} increases above three, the number of stable states begins to decline, with S2 becoming unstable for structures with four creases (point iv). For structures with five creases and above, only S1 remains stable at a compressive strain of 15%, although S3 is still stable under lower strains for n_{crease} = 5 and 6. This can be expected because we are approaching the continuous case when the number of creases is large.

The available stable states also depend strongly on the magnitude of the applied compressive strain used in the assembly process of the structure. We illustrate this using a structure with three creases due to its rich phenomena that will be discussed in the following. Based on the number and configurations of stable states, five regimes are identified: (a) two distinct stable states (S1 and S2; 0–10% strain), (b) three distinct stable states (S1, S2, and S3; 10–17% strain), (c) two distinct stable states (S1 and S3; 17–19% strain), (d) three distinct stable states (S1, S3, and S4; 19–30% strain), and (e) two distinct stable states (S1 and S4; 30–40% strain). Fig. 2C shows experimental and computational results of distinct stable states at representative strain levels for the five regimes. Under a relatively low compressive strain of 8% (point vi), states S1 (one center peak) and S2 (one side peak) exist, which can be reversibly reconfigured into each other via manually controlling the magnetic force and direction. Increasing the strain to 15% (point iii) leads to the appearance of a third state, S3 with two peaks, which increases the number of stable states to three. However, when the strain is further increased to 18% (point vii), S2 with one side peak disappears. Further increasing the strain to 24% (point viii) causes the formation of an interesting twisted state (S4) and therefore increases the number of stable states to three (S1, S3, and S4). As the strain becomes even larger, S3 disappears and only S1 and S4 exist at the strain of 34% (point ix). The experimental and computational results shown above agree reasonably well. The discrepancy in the configuration of some stable states (e.g., state S1 at point v in Fig. 2B) between experiments and modeling likely results from the friction between the structure and the substrate in experiments, which is neglected in computational modeling. The effect of friction will be further discussed in Section 2.3. Furthermore, by continuously changing the strain levels from 0% to 40% using the 3-crease structure, we record the dynamic progression of the five regimes and the fast, remote magnetic reconfiguration among the stable states within each regime in Movie S1 (ESI†), which is highly consistent with the predictions
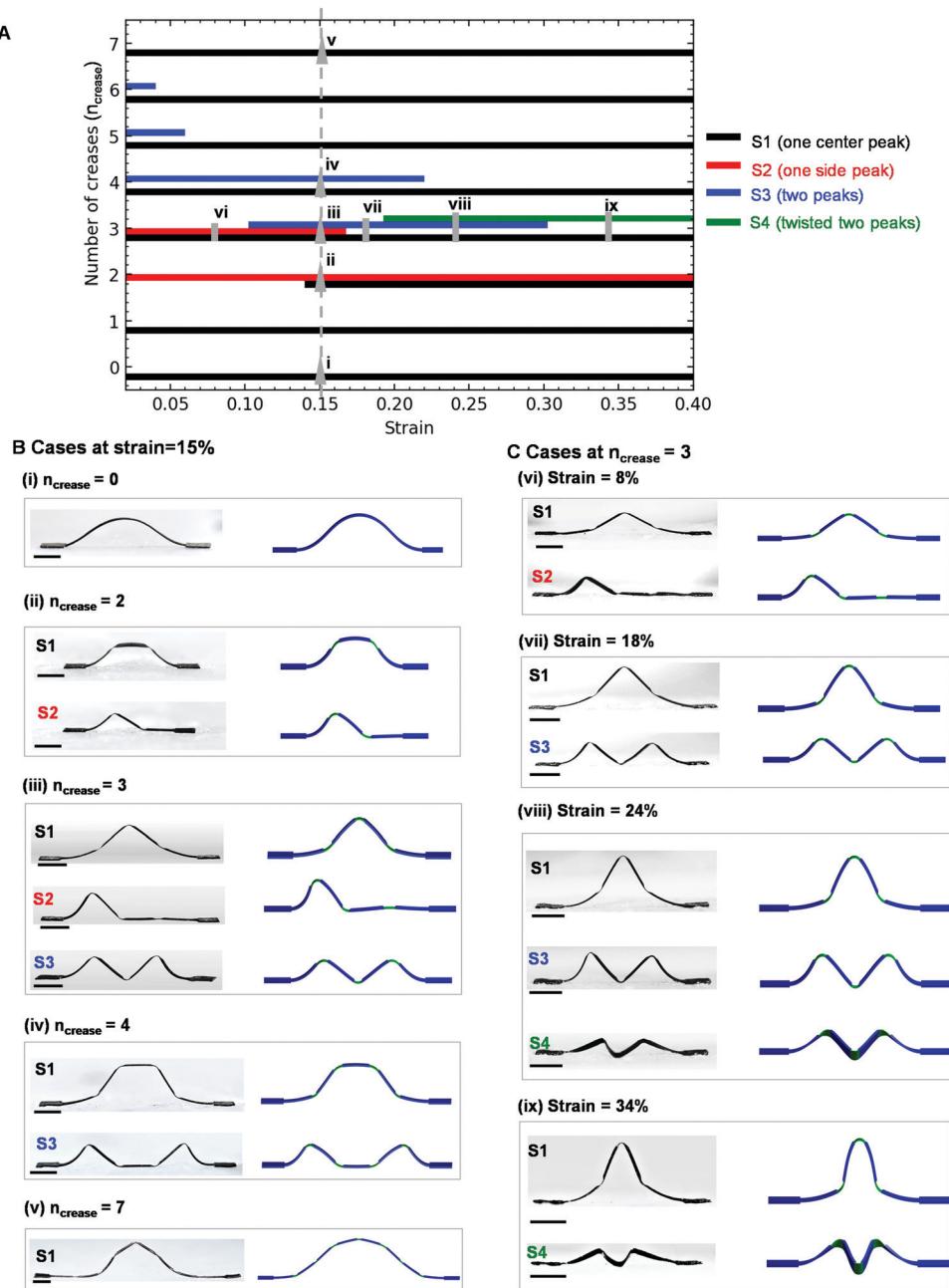
Fig. 2 Multistability of origami-inspired ferromagnetic ribbon structures under varying creases and compressive strains. (A) Design phase diagram showing the effect of the crease number and compressive strain on the number and configurations of distinct stable states of the ribbon. (B) Experimental and computational results of multistable states under a constant strain of 15% and varying crease numbers, corresponding to points i–v labelled in (A). Scale bars, 2 mm. (C) experimental and computational results of multistable states at a constant number of creases (n_{crease} = 3) and varying strain levels, corresponding to points (vi−ix) in (A). Scale bars, 2 mm.

of the design phase diagram in Fig. 2A. We also show that the states are stable under perturbations perpendicular to the vertical surface (along the height direction) of the ribbon, except in cases where S4 (twisted two peaks) is present. By using S1 as an example, the structure is shown to maintain its S1 configuration after the perturbations caused by a tweezer-induced external mechanical force (Fig. S1, ESI†).

The studies above provide important guidelines for tailoring the number and configurations of stable states in

origami-inspired structures by tuning the number of creases and the assembly strain. For example, for applications like in digital logic devices where multiple stable states are desired, structures with three creases may offer more design space and tunability, while structures with a lower or higher number of creases are preferred for applications where a single stable state is needed. Furthermore, from the design phase diagram, we observe that structures with two and three creases have multistable states under a wide range of strain (15–40% strain for the case of two creases and 0–40% strain

for the case of three creases), which can be used for applications of multistable structures that demand a wide working strain range. It is also worth emphasizing that a major advantage of employing the assembly strain as a control parameter is that varying strain levels and therefore tunable multistability can be repeatedly achieved by using a simple mechanical stage, as we will demonstrate later in Section 2.4.

We also study the effects of the crease thickness ratio and the crease length ratio (defined in Fig. S2, ESI†) on the multistability by using the 3-crease ribbon under a strain level of 14% as an example. Tables S1 and S2 (ESI†) show that both ratios have a significant effect on the multistability of the ribbon structure. In this work, we focus on the study of how the multistability can be tuned by the crease number and the strain levels. More detailed studies on the effects of the crease thickness ratio and the crease length ratio will be pursued elsewhere.

2.3 Reconfiguration paths among distinct stable states of origami-inspired ferromagnetic structures

In addition to locating the stable configurations, we also investigate available pathways that the structure can be reconfigured among its

stable states, which is important for many applications. The pathways are computationally identified by first locating the saddle points that connect the local minima on the energy landscape, also known as the transition states, using the so-called Binary Image Transition State Search model (see the Experimental section for the description of the algorithm). A full pathway is then given by the steepest-descent paths from the transition state to the energy minima, which are found by tracing the route of a minimization from each downhill side of the transition state.

Here we use the three-crease structure as a representative case for study because of its complexity in the configurations and the number of stable states, which results in a large number of reconfiguration paths. As illustrated in Fig. 3A, we identify four distinct pathways among the stable states of the structure: P_{1-2} for the transition path between S1 and S2, P_{1-3} between S1 and S3, P_{2-3} between S2 and S3, and P_{3-4} between S3 and S4. It is worth noting that in cases where one or more of those states are not stable, the corresponding individual paths may merge into one, as we will detail below.

Fig. 3B shows the available pathways and the associated energy profiles for a representative case in each of the five
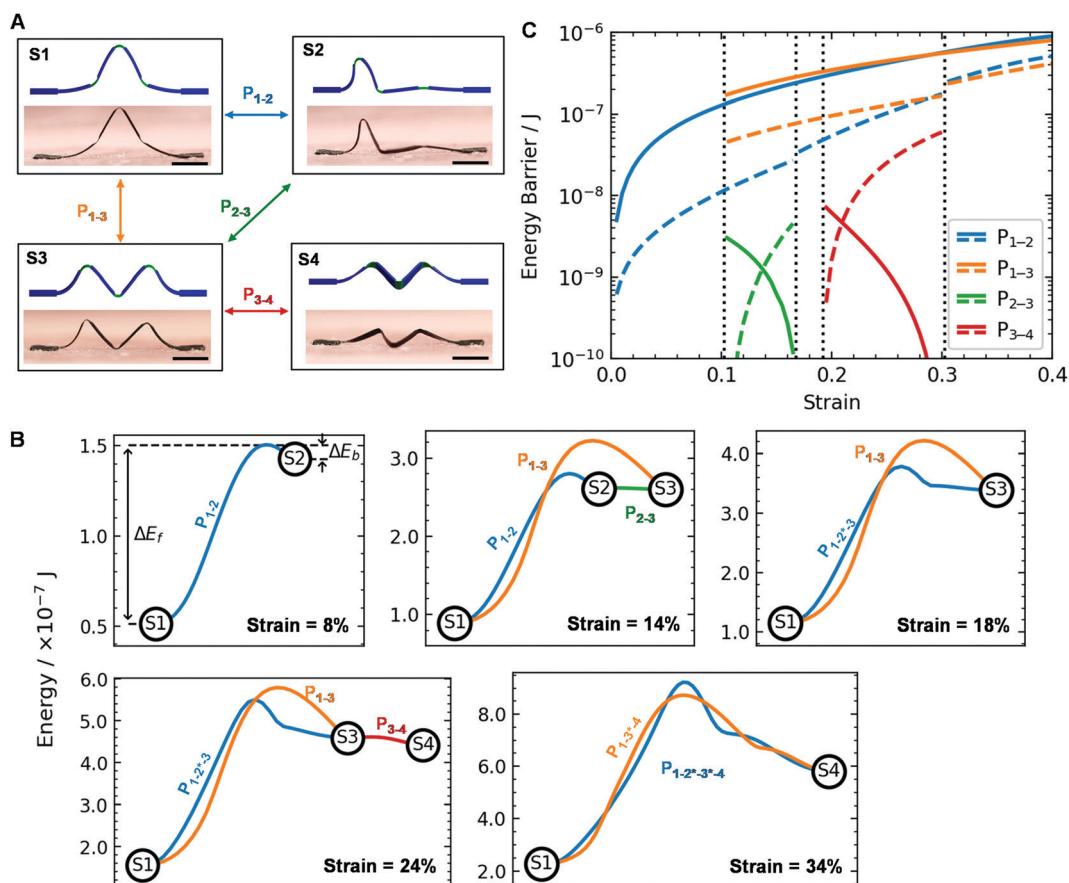
Fig. 3 Reconfiguration paths among distinct stable states of origami-inspired ferromagnetic ribbon structures. (A) Possible pathways between the stable states. Scale bars, 2 mm. (B) Energy profiles of pathways for the 3-crease ribbon structure at various strain levels. (C) Minimum energy barriers for pathways in Fig. 3B as a function of the strain. The solid lines indicate the energy barriers from the lower numbered states to the higher numbered states (illustrated by ΔE_f in (B)), and the dashed lines are the barriers from the higher numbered states to the lowered numbered states (illustrated by ΔE_b in (B)). Here, the line colors follow those of the pathways labelled in (A). The blue and orange lines also encompass the extended pathways P_{1-2*-3}, $P_{1-2*-3*-4}$, and P_{1-3*-4}.

regimes for a 3-crease ribbon (identified in Fig. 2A) as the strain is increased from 0% to 40%. In the first regime (0–10% strain), only states S1 and S2 exist, with a single pathway (P_{1-2}) to reconfigure between them, as shown in Movie S2 (ESI†). In the second regime (10–17% strain), state S3 appears, so two additional pathways, P_{1-3} and P_{2-3}, become accessible (Movie S3, ESI†). Our analysis also highlights that there are not only multiple stable states existing in the structure but also multiple available paths for transforming the structure from one state to another. For example, we can observe that there are two main pathways that can be taken from state S1 to S3. The first path, initially following P_{1-2} to reconfigure S1 to S2, subsequently involves the creation of an asymmetric peak at one side of the structure to form state S3 from S2 (P_{2-3}). Due to symmetry, there are two equivalent scenarios depending on which side the peak is created to form S3. The second path, P_{1-3}, directly reconfigures S1 to S3 by forming two edge peaks simultaneously while maintaining symmetry. As the strain increases to the regime of 17–19%, state S2 becomes unstable, so P_{1-2} and P_{2-3} merge into a single path P_{1-2*-3} (Movie S4, ESI†), where 2* denotes that state 2 is no longer stable. Above the strain of 19%, pathway P_{3-4} appears between state S3 and twisted state S4, while the two pathways from S1 to S3 still exist (Movie S5, ESI†). Finally, at the strain of 30% and above, S3 is no longer stable leaving just two merged paths $P_{1-2*-3*-4}$ and P_{1-3*-4} between S1 and S4 (Movie S6, ESI†), where 3* denotes that state S3 is no longer stable.

We further investigate the energy barriers of each pathway as a function of strain. For each pathway, there are two relevant energy barriers, as illustrated in Fig. 3B using P_{1-2} in the case of 8% strain as an example. We label ΔE_f for the energy required to transition from a lowered numbered state to a higher numbered state in each pathway (here, S1 to S2), while ΔE_b is the energy required for the opposite transition (here, S2 to S1). We summarize the values of the energy barriers for all the available pathways in Fig. 3C, where ΔE_f and ΔE_b for each pathway are represented by solid and dotted lines, respectively. We can see that the energy barriers for pathways reconfiguring from S1 to other states including S2, S3 and S4 depending on the strain levels (P_{1-2}, P_{1-2*-3}, $P_{1-2*-3*-4}$, P_{1-3}, P_{1-3*-4}; solid blue and orange lines) is much larger than their corresponding reverse barriers (dotted blue and orange lines, respectively). Such difference suggests that state S1 is more stable than the other states (S2, S3 and S4), which is consistent with the design phase diagram in Fig. 2A, where S1 is almost always stable for wide-ranging strains under all crease numbers. It is also seen that the energy barriers of paths P_{2-3} (green lines, transition between S2 and S3) and P_{3-4} (red lines, transition between S3 and S4) are significantly lower than those of pathways involving state S1 represented by solid blue and orange lines. This suggests that reconfigurations among states S2, S3, and S4 are much easier than those between S1 and S2/S3/S4. Correspondingly, the required forces to disturb the reconfiguration paths or trap locally stable states are low. Hence, forces like friction between the structure and the substrate (assembly platform) in experiments may be sufficient to trap the structure

along these paths for states S2, S3, and S4. This may explain why experimentally the structure appears to get trapped in some states which are shown to be unstable in computational results (Movies S4–S6, ESI†). For example, in Movie S4 (ESI†), when the structure is reconfigured from S2 to S3, the 2nd edge peak is not fully formed due to possible friction between the structure and the substrate, causing the slight asymmetric configuration of S3.

From Fig. 3C, we can also see that the energy barriers for the majority of the reconfiguration paths increase monotonically with the strain, implying that it becomes more difficult to reconfigure the states at larger strains. Exceptions occur for reconfiguration paths P_{2-3} (solid green line, transition from S2 to S3) and P_{3-4} (solid red line, transition from S3 to S4), the energy barriers of which decrease with increasing strain levels. Here, the cases when the energy barriers tend to be zero correspond to the instances where S2 and S3 become unstable, *i.e.*, the instability modes of these states. Overall, the energy barrier analysis reinforces the previous observation that, as the strain is varied from 0% to 40%, state S1 always exists for n_{crease} = 3 while the availability of states S2, S3 and S4 strongly depends on the strain imposed.

2.4 Origami-inspired multistable ferromagnetic structures of multi-ribbon configurations

The multistable ribbon configurations studied above can serve as building blocks for complicated geometries and diverse types of origami-inspired structures. Fig. 4A and Fig. S3 (ESI†) show a 3 × 3 array of ribbons with three creases at different strain levels, which is consistent with the prediction of the design phase diagram in Fig. 2A and demonstrates the scalability and versatility of the technique. Particularly, as predicted by the design phase diagram, three distinct stable states exist at the strain levels of 14% (S1, S2, and S3) and 28% (S1, S3, and S4), respectively. In experiments, each individual ribbon unit is separately addressable and therefore the structure array can be magnetically tuned in a sequential manner to display all the three stable states (S1 in row 1, S2 in row 2, and S3 in row 3 at a strain of 14%; S1 in column 1, S3 in column 2, and S4 in column 3 at a strain of 28%). Such capability of dynamically and reversibly tuning the patterns in a structure array represents an important option for applications including digital coding and smart switches,[9] especially when integrated with other functional materials or elements. In addition, the complexity of origami-inspired structures and the number of stable states can be increased by incorporating a larger number of interconnected structural units, like ribbons with two creases. Fig. 4B presents a structure consisting of two creased table structures connected by a creased ribbon, which can be magnetically reconfigured into six distinct stable states that are enabled by the multistability of the ribbon units. Furthermore, the multistable origami-inspired structures can be extended to diverse geometries. Fig. 4C and Fig. S4 (ESI†) demonstrate structures that mimic insect flexion, standing states, and a series of biomimetic movements. More examples including those that resemble two stable states of a butterfly, a cage, and a drug-release system are shown in Fig. S5 (ESI†).
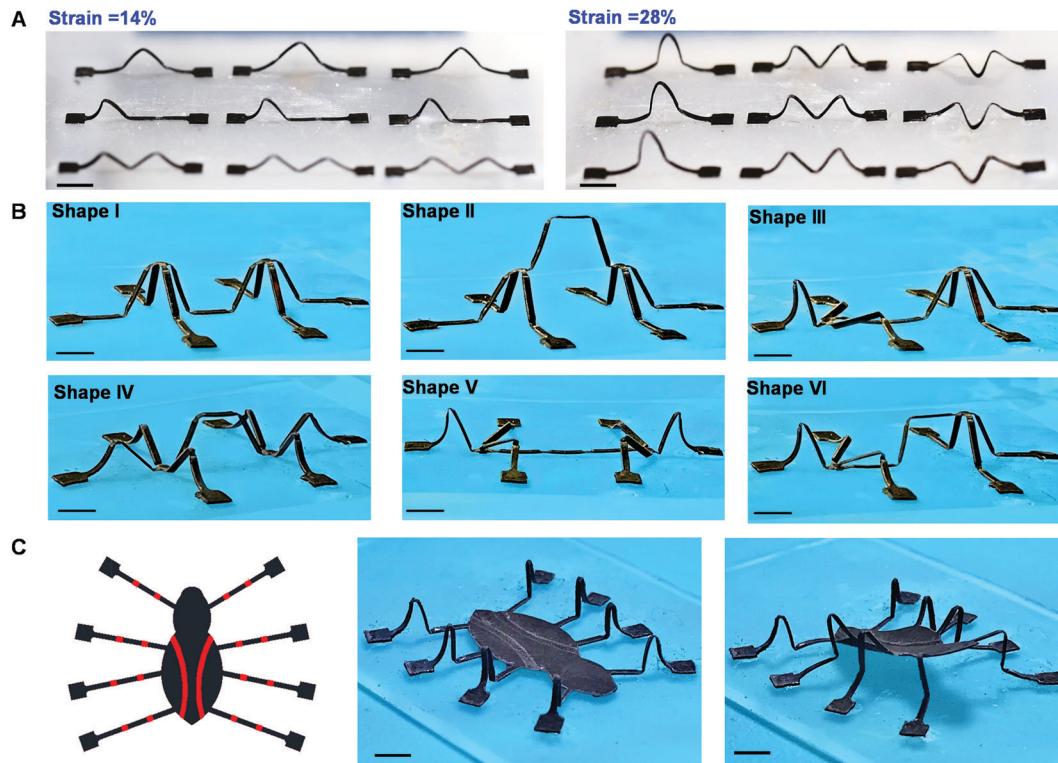
Fig. 4 Diverse origami-inspired, multistable ferromagnetic structures that can be actuated by magnetic forces. (A) An array of 3-crease ribbon structures showing different patterns formed by the multistable states of the ribbon under the strains of 14% and 28%, respectively. Scale bars, 3 mm. (B) Multistable states and magnetic reconfiguration of a double-table structure composed of creased ribbon segments. A strain of 30% is used for assembling the structure. Scale bars, 2 mm. (C) A multistable biomimetic "insect" in its flat and standing states, respectively. A strain of 30% is used for assembling the structure. Scale bars, 2 mm.

2.5 Application in soft robotics

Based on the multistability of origami-inspired structures and the flexibility of magnetic actuation, we further assemble two 3-crease ribbon structures (side by side) into a 3D origami robot to achieve a fast, remote response to an external magnetic field. Fig. 5A shows the design concept and assembly process, which begins with two buckled ferromagnetic ribbon structures of 3 creases (150 μm thick) attached to an elastomer substrate (400 μm thick). Each center peak of the two structures acts as the "foot" of the robot, which can drive the robot to move forward under magnetic actuation. To actuate the robot, a portable magnet is placed directly underneath the structure to bring the front "foot" forward, while the other one serves as a fulcrum at the back. Once the magnet is removed, the hinge on the front "foot" recovers its original shape, driving the robot forward. The actuation process above is recorded in Fig. 5B and Movie S7 (ESI†). Future opportunities include the fabrication and actuation of freestanding biomimetic structures by using the shape fixing effect of shape memory polymers,[19,49] or liquid crystal elastomers[50] for applications including remotely controlled soft robotics.

3. Conclusion

To sum up, we show from experiments and simulations that the multistability and the associated transition paths of origami-inspired, compressively buckled ferromagnetic structures can
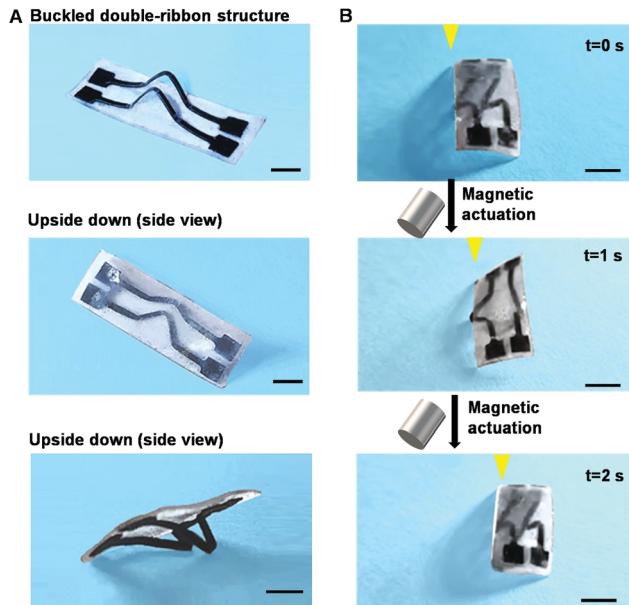
Fig. 5 An origami-inspired ferromagnetic robot composed of two ribbon structures of 3 creases. (A) Optical images of the robot. A strain of 25% is used for assembling the robot. Scale bars, 2 mm. (B) Motion behaviors of the robot under magnetic actuation. Scale bars, 2 mm.

be tailored by controlling the number of creases and assembly strain. Our constructed design phase diagram of a

representative creased ribbon structure from the energy landscape analysis is validated by our experiments and provides important guidelines for the targeted number of stable states by varying the two control factors. In addition, transition pathways among the distinct stable states are computed, and they illustrate how the structure can be manipulated to be reconfigured along different pathways. The experimental results of our origami-inspired ferromagnetic structures show targeted multistable states following designed pathways, which highly agrees with those from modeling. The fundamental understanding of the multistability of creased ribbon structures provides important guidelines for the design and application of complex classes of origami-inspired systems that are capable of multiple shape reconfigurations. Demonstrated examples include the arrays of creased ribbon units, a series of biomimetic states of a developed "insect" structure, and a soft robot based on a double-ribbon structure. These results highlight potential opportunities in the future to exploit multistable, origami-inspired ferromagnetic structures for intelligent and adaptive systems such as programmable digital logic arrays by integrating complex structure design and functional materials like stimuli-responsive polymers and electronics. It will also be interesting to explore the concept of actively manipulating the number of stable states and their reconfiguration paths in the design of other types of functional structures by using alternative control parameters.

4. Experimental section

Fabrication of 2D ferromagnetic composite precursors

The fabrication of ferromagnetic composite films began with using a planetary mixer (AR-100, Thinky) to homogeneously mix (2000 rpm for 2 min, then defoaming at 2000 rpm for 1 min) NdFeB (neodymium iron boron) microparticles (average diameter: 5 μm, Neo Magneuench) into uncured PDMS (polydimethylsiloxane, made with a volume ratio of part A over part B of 5:1) resin at a volume ratio of 1:5. Then the obtained ferromagnetic PDMS composite was spin coated onto a Petridish at 500 rpm for 15 s. The completely cured ferromagnetic film (thickness = 180–200 μm) was obtained after 2 days and laser cut into desired 2D patterns. The raster mode of the laser (VLS 2.30, Universal Laser System, Ansonia, CT) was used to create the crease segment of origami structures.

3D assembly

The assembly of origami-inspired structures was conducted using the previously introduced 3D buckling technique.[42] The 2D precursor was transferred onto a prestreched elastomer substrate (1 mm thick, Dragon Skin; Smooth-On, Easton, PA). Strong adhesion was formed at bonding sites by applying a thin layer of superglue. More specifically, a needle tip was used to apply a tiny drop of the superglue to the center of the bonding site, followed by physical lamination of the film onto the elastomer substrate to spread the superglue into a very thin layer. Releasing the prestrain in the assembly platform transformed the 2D pattern into a 3D structure and completed the assembly process.

Magnetic actuation

A cylinder magnet (D8Y0, K&J magnetics) was used to actuate the origami-inspired structures, and the ferromagnetic field was generated from the circular surface (diameter: 1.27 cm) of the cylinder magnet. The working distance of the magnet for effective actuation was identified to be 3–22 mm for this specific magnet. By adjusting the distance within this range and the angle (0–180°) between the circular surface and the targeted part of the structure, the strength and the direction of the applied ferromagnetic field were controlled to address the needs of reconfigurations.

Assembly of a soft robot

The 3D buckling technique was used for the assembly of a soft robot. 2D precursors of two ribbon structures with 3 creases were patterned from ferromagnetic composite films by using a laser (VLS 2.30, Universal Laser System, Ansonia, CT), which were then transferred onto a prestreched elastomer substrate (400 μm thick, Dragon Skin; Smooth-On, Easton, PA). Strong adhesion was formed at bonding sites by applying a thin layer of superglue. Releasing the prestrain in the assembly platform transformed the 2D patterns into origami structures (in a form of a 2 × 1 array) in their symmetric one-peak state (state S1). Then a laser was used to cut the substrate around the structure into a rectangle of 16 mm × 5 mm. The entire system was then turned upside-down.

Modeling

The structures were discretized as a 2D triangular mesh using a Delaunay refinement with an optimal mesh size equal to an eighth of the ribbon width. The energy of the structure was calculated by considering contributions from the stretching and bending of the mesh, as well as a repulsive potential with the substrate. A bar-and-hinge model was used for the stretching and bending components. This involved treating the bonds in the triangulation as elastic springs and with elastic hinges connecting adjacent triangular faces. The resulting expression for the energy is

$$E = \sum_b K_{S,b}\left(r_b - r_b^0\right)^2 + \sum_h K_{B,h}(1 + \cos\theta_h), \qquad (1)$$

where the summations are over each of the bonds, b, and hinges, h, respectively. For each bond, r_b is its length and r_b^0 is the relaxed length when in the 2D precursor, while θ_h is the dihedral angle of each hinge. The spring coefficients were obtained by considering the stiffness and flexural rigidities of the individual triangular elements. They are

$$K_{S,i} = \frac{\sqrt{3}}{4}Et_i, \qquad (2)$$

$$K_{B,i} = \frac{Et_i^3}{12(1-\nu^2)}\frac{r_i}{A_{i,1} + A_{i,2}}, \qquad (3)$$

where E is the Young's modulus, ν is the Poisson's ratio, t_i is the thickness, which is smaller at the creases, and $A_{i,1}$ and $A_{i,2}$ are the areas of the triangles at each side of the hinge. The values used were a Young's modulus of 1.4 MPa[51] and a thickness of 130 μm (for the ribbon stripes) or 60 μm (for the creases). As to the Poisson's ratio in eqn (3), the current discrete shell leads to a fixed value of $\nu = 1/3$,[34] smaller than the typical Poisson's ratio value for polymeric materials (~ 0.5). However, we do not expect this will significantly influence the results as the thin film deformation is mainly determined by the two stiffnesses (stretching and bending) defined in eqn (2) and (3). For the repulsive substrate interaction, each node in the triangulation was subject to a Lennard-Jones 9-3 potential which was shifted and cutoff to remove the attractive region:

$$E(r) = \varepsilon\left[\frac{2}{15}\left(\frac{\sigma}{r + r_0}\right)^9 - \left(\frac{\sigma}{r + r_0}\right)^3\right] - E_0 \quad \text{for } r < 0, \quad (4)$$

where r_0 is the distance at which the unshifted potential is minimal, and E_0 is the value of the potential at that location. The values used were $\sigma = 1$ mm and $\varepsilon = 10^{-10}$ J.

Finding stable states

The stable states correspond to configurations that lie at the local minima in the energy landscape, so they were found by minimizing the energy of the system. The L-BFGS algorithm was used for this because it is efficient for large numbers of degrees of freedom. To enable different states to be obtained, we carefully sampled the available states at selected points in the design phase diagram, typically at 5 different strain levels for each crease number. At such a point, random forces were applied to each of the creases and the structure was buckled by moving the binding sites according to the strain over the first 10 000 iterations, after which the structure was allowed to relax. This process was repeated several hundred times. Once the qualitatively distinct configurations were identified, the strain was then varied for each configuration to observe the range over which they were stable. To ensure our procedure is robust, we increased the sampling frequency of each configuration and we reliably found the same states.

Finding transition states

To identify the transition states for use in locating the pathways, the binary-image transition state search (BITSS) method was used. Briefly, this method used two states, denoted by x_1 and x_2, which were initialized at the two minima. The energy of this pair of states was then minimized subject to two constraints. Firstly, the distance between the two states was set as a value d_0, which was steadily reduced to zero such that the states converged at the transition state. The second constraint required the energies of the individual states, E_1 and E_2, to be equal. This prevented one state from passing over the saddle point, which would result in the convergence occurring at one of the minima instead. These two constraints were applied as penalty terms in the total energy to be minimized:

$$E_{\text{tot}}(x_1, x_2) = E_1 + E_2 + K_e(E_1 - E_2)^2 + K_d(d(x_1, x_2) - d_0)^2, \quad (5)$$

where $d(x_1, x_2)$ is the distance between the two states, defined by the root mean square separation between corresponding vertices in the two states; and K_e and K_d parametrize the strength of the constraints. These coefficients were computed at regular intervals as the separation d_0 was reduced so that all the energy terms remained relevant. The coefficient for the energy constraint was set by the expression $K_e = 10/\Delta E$, where ΔE is an estimate for the current energy barrier between x_1 and x_2, obtained by linearly interpolating between them. For a given d_0, the distance coefficient K_d was initially set as the reciprocal of the separation between the minima. If the states converge with a relative error in a distance from d_0 of greater than 1%, K_d would be increased by a factor of 10. This was repeated until the relative error was within 1%, in which case we then continued with the BITSS method with a smaller distance constraint. Typically, we reduce d_0 by 30%. After finding a transition state at a given strain parameter, a continuation approach can then be used in conjunction with the BITSS method to find the state for nearby parameters. By repeating this process, the transition states, and hence energy barriers, were identified for the whole parameter range of interest.

Conflicts of interest

The authors declare no competing financial interests.

Acknowledgements

References

1 Y. Chen, R. Peng and Z. You, *Science*, 2015, **349**, 396.
2 L. H. Dudte, E. Vouga, T. Tachi and L. Mahadevan, *Nat. Mater.*, 2016, **15**, 583–588.
3 X. Ning, X. Wang, Y. Zhang, X. Yu, D. Choi, N. Zheng, D. S. Kim, Y. Huang, Y. Zhang and J. A. Rogers, *Adv. Mater. Interfaces*, 2018, **5**, 1800284.
4 D. Thesiya, A. Srinivas and P. Shukla, *J. Astron. Instrum.*, 2015, **4**, 1550006.
5 D. Melancon, B. Gorissen, C. J. García-Mora, C. Hoberman and K. Bertoldi, *Nature*, 2021, **592**, 545–550.
6 M. Liu, L. Domino and D. Vella, *Soft Matter*, 2020, **16**, 7739–7750.
7 S. Felton, M. Tolley, E. Demaine, D. Rus and R. Wood, *Science*, 2014, **345**, 644–646.

8 J. L. Silverberg, A. A. Evans, L. McLeod, R. C. Hayward, T. Hull, C. D. Santangelo and I. Cohen, *Science*, 2014, **345**, 647–650.

9 T. Chen, M. Pauly and P. M. Reis, *Nature*, 2021, **589**, 386–390.

10 C. Yang, M. Boorugu, A. Dopp, J. Ren, R. Martin, D. Han, W. Choi and H. Lee, *Mater. Horiz.*, 2019, **6**, 1244–1250.

11 J. Hellmeier, R. Platzer, A. S. Eklund, T. Schlichthaerle, A. Karner, V. Motsch, M. C. Schneider, E. Kurz, V. Bamieh, M. Brameshuber, J. Preiner, R. Jungmann, H. Stockinger, G. J. Schutz, J. B. Huppa and E. Sevcsik, *Proc. Natl. Acad. Sci. U. S. A.*, 2021, **118**(4), DOI: 10.1073/pnas.2016857118.

12 K. Miura, *Inst. Space Astronaut. Sci. Rep.*, 1985, 1–9.

13 E. T. Filipov, T. Tachi and G. H. Paulino, *Proc. Natl. Acad. Sci. U. S. A.*, 2015, **112**, 12321–12326.

14 J. L. Silverberg, J. H. Na, A. A. Evans, B. Liu, T. C. Hull, C. D. Santangelo, R. J. Lang, R. C. Hayward and I. Cohen, *Nat. Mater.*, 2015, **14**, 389–393.

15 S. Sadeghi and S. Li, *Extreme Mech. Lett.*, 2020, **40**, 100958.

16 K. Liu, T. Tachi and G. H. Paulino, *Nat. Commun.*, 2019, **10**, 4238.

17 H. Fang, T.-S. Chang and K. W. Wang, *Smart Mater. Struct.*, 2019, **29**, 015026.

18 Z. R. Zhai, Y. Wang and H. Q. Jiang, *Proc. Natl. Acad. Sci. U. S. A.*, 2018, **115**, 2032–2037.

19 X. Wang, X. Guo, J. Ye, N. Zheng, P. Kohli, D. Choi, Y. Zhang, Z. Xie, Q. Zhang, H. Luan, K. Nan, B. H. Kim, Y. Xu, X. Shan, W. Bai, R. Sun, Z. Wang, H. Jang, F. Zhang, Y. Ma, Z. Xu, X. Feng, T. Xie, Y. Huang, Y. Zhang and J. A. Rogers, *Adv. Mater.*, 2019, **31**, e1805615.

20 Y. Liu, B. Shaw, M. D. Dickey and J. Genzer, *Sci. Adv.*, 2017, **3**, e1602417.

21 Q. Ge, C. K. Dunn, H. Qi and M. Dunn, *Smart Mater. Struct.*, 2014, **23**, 094007.

22 S. Janbaz, R. Hedayati and A. A. Zadpoor, *Mater. Horiz.*, 2016, **3**, 536–547.

23 A. S. Gladman, E. A. Matsumoto, R. G. Nuzzo, L. Mahadevan and J. A. Lewis, *Nat. Mater.*, 2016, **15**, 413–418.

24 Y. Zhang, X. Le, Y. Jian, W. Lu, J. Zhang and T. Chen, *Adv. Funct. Mater.*, 2019, **29**, 1905514.

25 A. Kotikian, C. McMahan, E. C. Davidson, J. M. Muhammad, R. D. Weeks, C. Daraio and J. A. Lewis, *Sci. Robot.*, 2019, **4**(33), DOI: 10.1126/scirobotics.aax7044.

26 Y. Li, H. Yu, K. Yu, X. Guo and X. Wang, *Adv. Funct. Mater.*, 2021, 2100338.

27 Y. Kim, H. Yuk, R. Zhao, S. A. Chester and X. Zhao, *Nature*, 2018, **558**, 274–279.

28 M. Jamal, S. S. Kadam, R. Xiao, F. Jivan, T.-M. Onn, R. Fernandes, T. D. Nguyen and D. H. Gracias, *Adv. Healthcare Mater.*, 2013, **2**, 1142–1150.

29 S. Chen, J. Chen, X. Zhang, Z.-Y. Li and J. Li, *Light: Sci. Appl.*, 2020, **9**, 75.

30 L. Xu, T. C. Shyu and N. A. Kotov, *ACS Nano*, 2017, **11**, 7587–7599.

31 L. S. Novelino, Q. Ze, S. Wu, G. H. Paulino and R. Zhao, *Proc. Natl. Acad. Sci. U. S. A.*, 2020, **117**, 24096.

32 W. Xu, Z. Qin, C. T. Chen, H. R. Kwag, Q. Ma, A. Sarkar, M. J. Buehler and D. H. Gracias, *Sci. Adv.*, 2017, **3**, e1701084.

33 S. Xu, Z. Yan, K.-I. Jang, W. Huang, H. Fu, J. Kim, Z. Wei, M. Flavin, J. McCracken and R. J. S. Wang, *Science*, 2015, **347**, 154–159.

34 H. Seung and D. R. Nelson, *Phys. Rev. A: At., Mol., Opt. Phys.*, 1988, **38**, 1005.

35 E. Grinspun, A. N. Hirani, M. Desbrun and P. Schröder, *ACM/Eurographics Symposium on Computer Animation*, 2003, pp. 62–67.

36 C. J. Pickard and R. J. Needs, *J. Phys.: Condens. Matter*, 2011, **23**, 053201.

37 J. Chen, G. Schusteritsch, C. J. Pickard, C. G. Salzmann and A. Michaelides, *Phys. Rev. Lett.*, 2016, **116**, 025501.

38 H. Zhang, X. Cheng, D. Yan, Y. Zhang and D. Fang, *Compos. Sci. Technol.*, 2019, **183**, 107822.

39 J. Panter, J. Chen, T. Zhang and H. Kusumaatmaja, *Commun. Phys.*, 2019, **2**, 1–9.

40 E. Weinan, W. Ren and E. Vanden-Eijnden, *J. Chem. Phys.*, 2007, **126**, 164103.

41 Y. Li, S. Avis, J. Chen, G. Wu, T. Zhang, H. Kusumaatmaja and X. Wang, *Extreme Mech. Lett.*, 2021, **48**, 101428.

42 Y. H. Zhang, Z. Yan, K. W. Nan, D. Q. Xiao, Y. H. Liu, H. W. Luan, H. R. Fu, X. Z. Wang, Q. L. Yang, J. C. Wang, W. Ren, H. Z. Si, F. Liu, L. H. Yang, H. J. Li, J. T. Wang, X. L. Guo, H. Y. Luo, L. Wang, Y. G. Huang and J. A. Rogers, *Proc. Natl. Acad. Sci. U. S. A.*, 2015, **112**, 11757–11764.

43 Y. Liu, X. Wang, Y. Xu, Z. Xue, Y. Zhang, X. Ning, X. Cheng, Y. Xue, D. Lu, Q. Zhang, F. Zhang, J. Liu, X. Guo, K. C. Hwang, Y. Huang, J. A. Rogers and Y. Zhang, *Proc. Natl. Acad. Sci. U. S. A.*, 2019, **116**, 15368–15377.

44 W. Hu, G. Z. Lum, M. Mastrangeli and M. Sitti, *Nature*, 2018, **554**, 81–85.

45 S. Wu, W. Hu, Q. Ze, M. Sitti and R. Zhao, *Multifunct. Mater.*, 2020, **3**, 042003.

46 D. Yan, M. Pezzulla, L. Cruveiller, A. Abbasi and P. M. Reis, *Nat. Commun.*, 2021, **12**, 2831.

47 Y. Tang, Y. Li, Y. Hong, S. Yang and J. Yin, *Proc. Natl. Acad. Sci. U. S. A.*, 2019, **116**(52), 26407–26413.

48 W. Huang, Y. Wang, X. Li and M. K. Jawed, *J. Mech. Phys. Solids*, 2020, **145**, 104168.

49 Y. Li, C. Luo, K. Yu and X. Wang, *ACS Appl. Mater. Interfaces*, 2021, **13**, 8929–8939.

50 T. H. Ware, M. E. McConney, J. J. Wie, V. P. Tondiglia and T. J. White, *Science*, 2015, **347**, 982–984.

51 Y. Kim, G. A. Parada, S. Liu and X. Zhao, *Sci. Robot.*, 2019, **4**(33), DOI: 10.1126/scirobotics.aax7329.